21st Australasian Fluid Mechanics Conference
Adelaide, Australia
10-13 December 2018

Experimental Flow Reconstruction Using Resolvent Analysis and Data-Assimilation

S. Symon[1] **and B. J. McKeon**[1]

[1]Graduate Aerospace Laboratories
California Institute of Technology, Pasadena, CA 91125, USA

Abstract

A flow reconstruction methodology utilizing resolvent analysis and data-assimilation is applied to flow around a NACA 0018 airfoil at an angle of attack $\alpha = 10^\circ$ and chord-based Reynolds number $Re = 10250$. The underlying principle of the reconstruction is to maximize the value of limited experimental measurements as the only inputs are a rough approximation of the mean profile and two time-resolved probes. The input data may be incomplete, in the sense that measurements near a body are difficult to obtain with techniques such as particle image velocimetry (PIV), or contaminated by noise. The final reconstruction contains less measurement noise compared to the PIV data and obeys the incompressible Navier-Stokes equations (NSE).

Introduction

A growing number of studies have used the time-averaged flow, or the mean, and limited time-resolved measurements to reconstruct statistically stationary flows. The mean can be used as an input to the resolvent analysis of [6], which recasts the Navier-Stokes equations as a closed-loop system. The linear dynamics act as a directional amplifier and are forced by the nonlinear interaction of velocity modes. A singular value decomposition (SVD) of the resolvent operator ranks the dominant coherent structures at a given temporal frequency by their gain or singular value. Quite often, the leading singular value is significantly larger than the others, a feature exploited by [4] and [1] to compute the structure at a given frequency without resorting to data-driven methods. The amplitude and phase, or complex weight, of the response modes was determined using a single time-resolved measurement in an energetic region of the flow.

A similar reconstruction procedure was adapted by [2] for transitional jets and [10] for a NACA 0012 airfoil at a non-zero angle of attack. However, there are limitations to this method, some of which have been discussed by [11] and [8]. If the nonlinear forcing is not white in noise and time, for example, a low-order representation by resolvent modes is not likely to predict structures which agree with modes computed from data. It is also assumed that knowledge of the mean profile is available everywhere, but this might not be the case with experimental data. The focus here is on applying data-assimilation, a technique whereby experimental measurements are merged with computational fluid dynamics [5], to address one limitation of the methodology outlined in figure 1. The mean flow around a NACA 0018 airfoil at $\alpha = 10^\circ$ and $Re = 10250$ is obtained by time-averaging PIV data. It is then data-assimilated to fill in missing data and extrapolate beyond the PIV domain before being used as an input to resolvent analysis. The resolvent modes are computed and calibrated using time-resolved measurements to reconstruct the unsteady velocity fields.

Methods

Experimental Setup

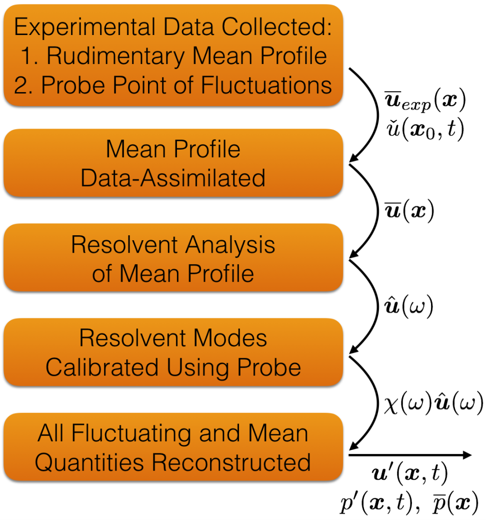

Figure 1: A schematic inspired by [2] of the flow reconstruction procedure.

PIV data are collected for a NACA 0018 airfoil with a chord length of 10 cm and a spanwise extent of 48 cm at a chord-based Reynolds number of $Re = 10250$ and an angle of attack of $\alpha = 10^\circ$. A LaVision time-resolved 2D PIV setup is used consisting of two Phantom Miro 320 cameras with 50 mm focal length Nikon lenses and 1:1.8 aperture. They have an overlap of 18% in the streamwise direction and sample the flow at a frequency of 125 Hz. The cameras' resolution is 1920×1200 pixels and they are calibrated at 8.2 px/mm. The laser sheet is provided by a YLF dual cavity solid-state laser and is centered at a height of 220 mm.

Velocity vectors are computed using the software package DaVis provided by LaVision. A standard cross-correlation technique via Fast Fourier Transformation is applied to each sequential image with a window-size reduced from 64×64 px^2 to 32×32 px^2 over three passes, a 50% overlap, and a 2:1 elliptic weight. Finally, the data are post-processed and single missing vectors are interpolated using an average of all the nonzero neighborhood vectors. 7,000 snapshots are collected and these are averaged in time to obtain the mean velocity profile and Reynolds stresses.

Data-Assimilation

The experimental application of the data-assimilation framework introduced by [3] is described in detail by [9] so only the equations are summarized here. To begin with, the incompressible NSE are non-dimensionalized by the free-stream velocity and airfoil chord such that they can be written as

$$\partial_t \mathbf{u} + \mathbf{u} \cdot \nabla \mathbf{u} = -\nabla p + Re^{-1} \nabla^2 \mathbf{u} \tag{1}$$

$$\nabla \cdot \mathbf{u} = 0. \tag{2}$$

After Reynolds decomposing the field into a mean and fluctuation, i.e., $\mathbf{u} = \overline{\mathbf{u}} + \mathbf{u}'$, one obtains the incompressible RANS equations which the data-assimilated field must satisfy:

$$\overline{\mathbf{u}}\cdot\nabla\overline{\mathbf{u}}+\nabla\overline{p}-Re^{-1}\nabla^2\overline{\mathbf{u}}=\mathbf{f} \tag{3}$$

$$\nabla\cdot\overline{\mathbf{u}}=0, \tag{4}$$

where $\mathbf{f}$ is the divergence of the Reynolds stress tensor. It is assumed that only $\overline{\mathbf{u}}$ is known *a priori* from experiment and $\mathbf{f}$ is obtained by solving the constrained optimization problem

$$\mathcal{L}=\mathcal{E}-\left\langle\overline{\mathbf{u}}^{\dagger},\overline{\mathbf{u}}\cdot\nabla\overline{\mathbf{u}}+\nabla\overline{p}-Re^{-1}\nabla^2\overline{\mathbf{u}}-\mathbf{f}\right\rangle-\left\langle\overline{p}^{\dagger},\nabla\cdot\overline{\mathbf{u}}\right\rangle, \tag{5}$$

where $(\cdot)^{\dagger}$ denotes an adjoint quantity and $\langle\mathbf{a},\mathbf{b}\rangle=\int_{\Omega}\mathbf{a}\cdot\mathbf{b}\,d\Omega$. The scalar $\mathcal{E}$ penalizes the difference between the experimental mean profile $\overline{\mathbf{u}}_{exp}$ and $\overline{\mathbf{u}}$ which satisfies equation (3)

$$\mathcal{E}(\overline{\mathbf{u}})=\frac{1}{2}\|\overline{\mathbf{m}}-\mathcal{M}(\overline{\mathbf{u}})\|_M^2. \tag{6}$$

The quantity $\overline{\mathbf{m}}$ represents the measurements available from the PIV while the operator $\mathcal{M}$ projects the numerical data onto the measurement subspace M, which is generally of much lower dimension. The variational derivatives of $\mathcal{L}$ with respect to the forward and adjoint states yield the equations which are solved iteratively to update $\mathbf{f}$ until $\mathcal{L}$ is minimized, yielding the best assimilated mean.

Resolvent Analysis

The fluctuation equations are written such that the nonlinear terms are treated as a forcing term

$$\partial_t\mathbf{u}'+\overline{\mathbf{u}}\cdot\nabla\mathbf{u}'+\mathbf{u}'\cdot\nabla\overline{\mathbf{u}}+\nabla p'-Re^{-1}\nabla^2\mathbf{u}'=\mathbf{f}' \tag{7}$$

$$\nabla\cdot\mathbf{u}'=0, \tag{8}$$

where $\mathbf{f}'=-\mathbf{u}'\cdot\nabla\mathbf{u}'+\overline{\mathbf{u}'\cdot\nabla\mathbf{u}'}$. If the flow is stationary, equation (7) is Fourier-transformed in time and rearranged to yield a transfer function between a disturbance $\hat{\mathbf{f}}$ and a velocity response $\hat{\mathbf{u}}$

$$\hat{\mathbf{u}}=\mathbf{C}^T(i\omega\mathbf{B}-\mathbf{L})^{-1}\mathbf{C}\hat{\mathbf{f}}=\mathcal{H}(\omega)\hat{\mathbf{f}}, \tag{9}$$

where $\mathcal{H}(\omega)$ is the resolvent operator, $\mathbf{C}=(1\ 0)^T$, $\mathbf{B}=\mathbf{C}\mathbf{C}^T$, and $\mathbf{L}$ is the linear Navier-Stokes operator. It should be noted that the only input required for this analysis is the data-assimilated mean profile, which is solved for on the entire computational domain as opposed to the experimental mean.

A singular value decomposition (SVD) of the resolvent operator results in

$$\mathcal{H}(\omega)=\sum_{j=1}^{\infty}\hat{\psi}_j(\omega)\sigma_j(\omega)\hat{\phi}_j(\omega), \tag{10}$$

where $\hat{\psi}_j$ is the *jth* resolvent response mode with a gain of σ_j. The shape of the disturbance which most effectively triggers this velocity response is given by the associated resolvent forcing mode $\hat{\phi}_j$. In many instances, the gain associated with the first mode is significantly larger than the other singular values signifying that equation (10) can be approximated as

$$\mathcal{H}(\omega)\approx\sigma_1(\omega)\hat{\psi}_1(\omega)\hat{\phi}_1^*(\omega). \tag{11}$$

The linear operators needed to obtain the most amplified resolvent modes are formed in FreeFem++ and are computed using the procedure outlined in [7].

Reconstruction Procedure

Resolvent analysis does not supply the complex amplitude of each response mode which can be computed by projecting the forcing modes onto the nonlinear forcing

$$\hat{\mathbf{u}}(\omega)=\sum_j\hat{\psi}_j(\omega)\sigma_j(\omega)\left\langle\hat{\mathbf{f}}(\omega),\hat{\phi}_j(\omega)\right\rangle=\sum_j\hat{\psi}_j\sigma_j\overline{\chi}_j, \tag{12}$$

where the functional dependence on ω was omitted on the right-hand side for conciseness. Since $\hat{\mathbf{f}}$ is unknown, only the first resolvent response mode is computed due to the low-rank nature of $\mathcal{H}(\omega)$ and its weight $\chi_1=\sigma_1\overline{\chi}_1$ is computed using a velocity probe located in an energetic region of the flow $\mathbf{x}_0$. Following [4], the signal $\breve{u}(t,\mathbf{x}_0)$ is Fourier-transformed in time to predict the amplitude of the corresponding resolvent mode through the following expression:

$$\chi_1(\omega)=\hat{u}(\omega,\mathbf{x}_0)/\breve{u}(\omega,\mathbf{x}_0). \tag{13}$$

As explained by [4], it is possible to use more than one probe point in the flow and solve the overdetermined set of equations using a least-squares approach.

Results

Assimilated Flow

The u-component of the data-assimilated mean is compared to its PIV equivalent in figure 2. The agreement between the fields is generally very good and there are two noticeable improvements after the assimilation process. First, the data near the separation point (dashed green box) is filled where there is insufficient seeding density and resolution to capture the flow. Second, the PIV mean field consists of two means ($\alpha=\pm10°$) which are stitched together since the airfoil obstructs the laser sheet on one side. The data-assimilation is able to improve the stitching which is faintly visible near the trailing edge of the airfoil (dashed-dotted green box).

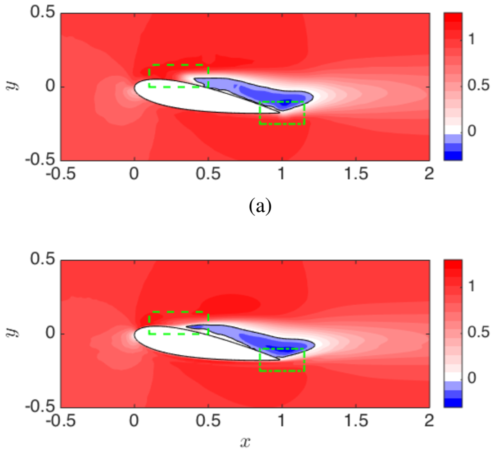

(a)

(b)

Figure 2: (a) PIV mean field and (b) data-assimilated mean field. The black line represents the $\overline{u}=0$ contour and demarcates the recirculation bubble.

Amplification Mechanisms

The first two singular values are computed for the experimental and data-assimilated profiles to identify the primary amplification mechanisms and the frequency ranges where the rank-1 approximation is appropriate. The experimental profile is interpolated onto a FreeFem mesh and, in regions outside the PIV domain, the velocity is set to $\overline{\mathbf{u}}=[1\ 0]^T$. The no-slip boundary condition is manually enforced along the airfoil surface. The results over a range of ω are plotted in figure 3. Both curves contain a peak around $\omega=6.5$ while only the data-assimilated peak contains a peak around $\omega=15$. Moreover, the range of frequencies where $\sigma_1\gg\sigma_2$ is far wider for the data-assimilated profile than it is for the experimental one.

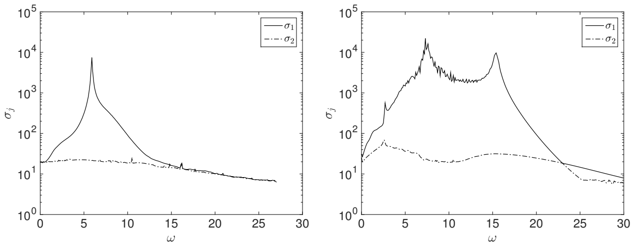

(a) (b)

Figure 3: First two singular values plotted as a function of ω for the (a) experimental and (b) data-assimilated means.

The mode shapes are plotted for three frequencies corresponding to the two peaks in figure 3(b) as well as an intermediate frequency at $\omega = 12$. Two linear mechanisms can be identified from the mode shapes in figure 4. The first corresponds to wake modes which occur at lower temporal frequencies as seen in figure 4(a). The second corresponds to shear layer modes which occur at higher temporal frequencies as seen in figure 4(c). The mode shapes for intermediate frequencies have a mix of both linear mechanisms as seen for the $\omega = 12$ mode in figure 4(b), which has activity both in the shear layer and the wake. These results are consistent with [10] and [12], who computed resolvent modes for a NACA 0012 airfoil at a similar Reynolds number and angle of attack. The latter study also identified two branches in the spectrum which were categorized as wake modes or shear layer modes.

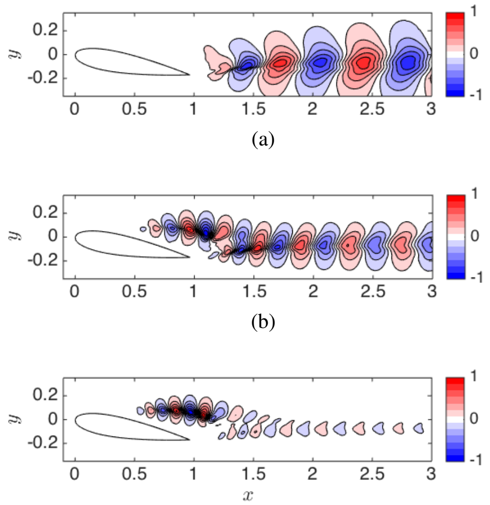

(a)

(b)

(c)

Figure 4: Optimal resolvent response modes for (a) $\omega = 7.3$, (b) $\omega = 12.0$, and (c) $\omega = 15.4$ using the data-assimilated mean.

Flow Reconstruction

The results from the previous section highlight the benefit of data-assimilating the experimental mean, which failed to identify the amplification mechanism associated with the shear layer due to missing PIV vectors near the separation point. The modes shapes obtained from resolvent analysis of the data-assimilated mean are utilized to approximate the full flow field. The probe points, which are used to calibrate the amplitude of the resolvent modes, are shown in figure 5 and measure v'. These have been chosen specifically to capture energetic regions of the flow where the dynamics associated with the shear layer (point 1) and the wake (point 2) are present.

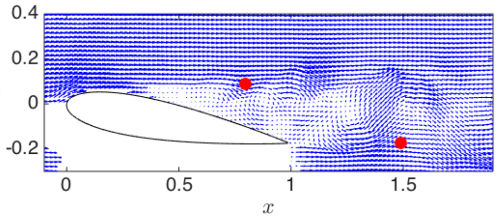

Figure 5: Locations (red dots) of probe point 1 in the shear layer and probe point 2 in the wake. The plot also contains PIV vectors to visualize the vortical regions in the flow.

The power spectra for the two probe points are presented in figure 6. The result in figure 6(a) is similar to the resolvent norm in figure 3(b) in that there are two main peaks around which the fluctuation energy is concentrated. The power spectrum in figure 6(b) illustrates how the fluctuation energy becomes almost exclusively concentrated in the wake modes further downstream. A single probe point in this location, therefore, is unlikely to successfully reconstruct the flow further upstream where there is more energy in higher frequency modes.

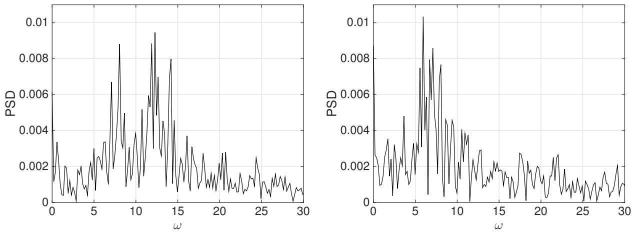

(a) (b)

Figure 6: Power spectrum at (a) point 1 and (b) point 2.

Three cases are compared where the flow is reconstructed using a probe located at point 1 only, point 2 only, and both points 1 and 2. Quantitive comparisons among these cases are made using the error metrics outlined in [2]. The instantaneous error $I_v(t)$ is

$$I_v(t) = \sqrt{\frac{1}{N}\sum_{i=1}^{N}(v^i(t) - v^i_{ref}(t)^2}, \tag{14}$$

where v denotes only the transverse velocity component is being considered, N is the number of discrete points where the velocity is known, and the reference field is the PIV snapshot. The global error E_v is obtained by integrating equation (14) in time to obtain

$$E_v = \frac{1}{T}\int_0^T I(t)dt. \tag{15}$$

The reconstructed flow using both points is compared to the raw PIV snapshot (no filtering) for $t = 4.82$ in figure 7. The resolvent-based reconstruction captures several flow features quite well. The agreement in the shear layer region ($0.5 < x < 1.5$), for example, is very good although the fluctuation levels in the PIV are slightly higher. The model is also capable of capturing the transition from the shear layer dynamics to the wake dynamics around the trailing edge where the wavelength of the fluctuations increases substantially immediately behind the airfoil. The model also shows these two mechanisms interacting in the region ($1 < x < 1.5$).

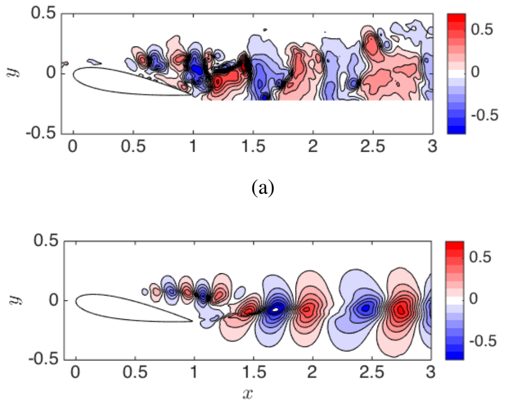

(a)

(b)

Figure 7: $v'(t = 4.82)$ for the (a) PIV snapshot and (b) resolvent-based model.

The performance of the model is poorer in the wake region. While it does correctly capture the correct wavelengths, it tends to overestimate the intensity of the fluctuations. This is most likely due to the fact that the wake dynamics are more reminiscent of oscillator-type behavior where the nonlinear forcing is structured and cannot be assumed to be white in noise and time. The shear layer dynamics, on the other hand, are more reminiscent of amplifier-type behavior where unstructured forcing is a more reasonable assumption. We have not included frequencies where the rank-1 approximation is not valid ($\omega > 20$) and so the finer scale structures are filtered out.

Finally, the performance of the model using just one point instead of both points is evaluated by computing E_v for each case. The results are summarized in table 1. The best performing case, not surprisingly, is using both points 1 and 2 while the worst performing case is the use of only point 1. One point is suboptimal since there are two mechanisms leading to amplification and peaks in the local power spectra. In figure 6(a), for example, the bulk of the fluctuation energy is concentrated around frequencies corresponding to the shear layer dynamics. When only point 1 is used, therefore, the model is overfitting the amplitudes to these higher frequencies resulting in a gross overestimation of the fluctuations behind the airfoil. In a similar manner, the power spectrum of point 2 has peaks exclusively centered around wake modes. The resulting model, therefore, predicts no fluctuations in the shear layer. Since the two linear mechanisms are well separated in physical space, it is difficult to select a single point which can accurately capture the fluctuations associate with both linear mechanisms and so the use of two points significantly outperforms the use of just one.

Error E_v		
Point 1	Point 2	Points 1 + 2
1.70	0.0416	0.0266

Table 1: Global error as a function of point selection.

Conclusions

The flow around a NACA 0018 airfoil at $\alpha = 10^\circ$ and $Re = 10250$ has been reconstructed using resolvent analysis and data-assimilation. Even though the PIV mean velocity field contained defects such as missing data near the leading edge and errors in the stitching process, the data-assimilation was able to correct these defects and extrapolate the mean field such that a global analysis could be conducted. The largest singular value of the data-assimilated mean recovered two peaks, highlighting the role of two linear mechanisms, whereas the experimental mean contained a single peak. The first was associated with the shear layer at high frequencies while the second was associated with wake modes. Two time-resolved probes were selected in regions where both linear mechanisms were energetic leading to considerable improvement in the reconstruction compared to the use of a single point.

Acknowledgements

The authors would like to acknowledge the financial support of the Army Research Office (Grant No. W911NF-17-1-0306) and the Office of Naval Research (Grant No. N00014-17-1-3022).

References

[1] Beneddine, S., Sipp, D., Arnault, A., Dandois, J. and Lesshafft, L., Conditions for validity of mean flow stability analysis, *J. Fluid Mech.*, **798**, 2016, 485–504.

[2] Beneddine, S., Yegavian, R., Sipp, D. and Leclaire, B., Unsteady flow dynamics reconstruction from mean flow and point sensors: an experimental study, *J. Fluid Mech.*, **824**, 2017, 174–201.

[3] Foures, D. P. G., Dovetta, N., Sipp, D. and Schmid, P. J., A data-assimilation method for Reynolds-averaged Navier-Stokes-driven mean flow reconstruction, *J. Fluid Mech.*, **759**, 2014, 404–431.

[4] Gómez, F., Blackburn, H. M., Rudman, M., Sharma, A. S. and McKeon, B. J., A reduced-order model of three-dimensional unsteady flow in a cavity based on the resolvent operator, *J. Fluid Mech.*, **798**, 2016, R2.

[5] Hayase, T., Numerical simulation of real-world flows, *Fluid Dyn. Res.*, **47**, 2015, 051201.

[6] McKeon, B. J. and Sharma, A. S., A critical-layer framework for turbulent pipe flow, *J. Fluid Mech.*, **658**, 2010, 336–382.

[7] Sipp, D. and Marquet, O., Characterization of noise amplifiers with global singular modes: the case of the leading-edge flat-plate boundary layer, *Theor. Comput. Fluid Dyn.*, **27**, 2013, 617–635.

[8] Symon, S., *Reconstruction and estimation of flows using resolvent analysis and data-assimilation*, Ph.D. thesis, California Institute of Technology, 2018.

[9] Symon, S., Dovetta, N., McKeon, B. J., Sipp, D. and Schmid, P. J., Data assimilation of mean velocity from 2D PIV measurements of flow over an idealized airfoil, *Exp. in Fluids*, **58**, 2017, 61.

[10] Thomareis, N. and Papadakis, G., Resolvent analysis of separated and attached flows around an airfoil at transitional Reynolds number, *Phys. Rev. Fluids*, **3**, 2018, 073901.

[11] Towne, A., Schmidt, O. T. and Colonius, T., Spectral proper orthogonal decomposition and its relationship to dynamic mode decomposition and resolvent analysis, *J. Fluid Mech.*, **847**, 2018, 821–867.

[12] Yeh, C.-A. and Taira, K., Resolvent-analysis-based design of airfoil separation control, *arXiv:1805.02128v1*.